ACS APPLIED MATERIALS & INTERFACES

www.acsami.org

Research Article

Manipulating Bulk Diffusion and Doping of Phosphomolybdic Acid Enables Organic Solar Cells with Improved Homogeneity

Jinlong Wu, Qian Xi, Na Wu, Rong Huang, Yi Lin,* and Chang-Qi Ma*

Cite This: *ACS Appl. Mater. Interfaces* 2025, 17, 40605−40612

Read Online

ACCESS | Metrics & More | Article Recommendations | Supporting Information

ABSTRACT: The application of organic solar cells (OSCs) significantly contributes to the advancement of sustainable development and the utilization of eco-friendly energy sources. The solution-based phosphomolybdic acid (PMA) doping method has been demonstrated to be effective in simplifying the fabrication of the hole transport layer (HTL) by modulating the optoelectronic properties of the photoactive layer (PAL). Here, the PMA doping method was applied to the state-of-the-art PM6:L8-BO-based OSCs. By laser beam-induced current (LBIC) and time-of-flight-secondary ion mass spectrometry (ToF-SIMS) measurements, we demonstrated that the diffusion of PMA is inhomogeneous with the PM6:L8-BO layer, which yielded poor device performance and broad distribution of power conversion efficiency (PCE) of the cells. To address this issue, a two-step spin-rinsing technique was developed that improved the homogeneity of PMA bulk diffusion over the PAL, leading to significantly improved device performance and narrowed PCE distribution. Most interestingly, this two-step procedure enables manipulation of the vertical diffusion of PMA. This is particularly important in thicker PAL solar cells. The optimized PM6:L8-BO cells with a PAL thickness of 280 nm exhibited an average PCE of 12.96%, which is 0.77% higher than that of the cell with thermal evaporated MoO_3 HTL.

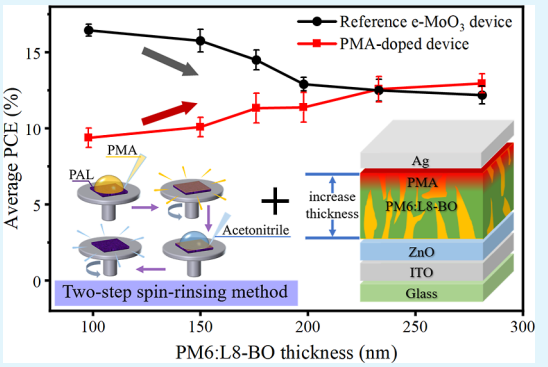

KEYWORDS: *organic solar cells (OSCs), phosphomolybdic acid (PMA), hole transport layer (HTL), solution-based method, doping, interface*

1. INTRODUCTION

Organic solar cells (OSCs), which have advantages including light weight,[1] low cost,[2] and large-area fabrication by the solution method,[3,4] may hold promise for advancing sustainable development and promoting the utilization of eco-friendly energy sources.[5] The configurations of OSCs are typically classified into conventional and inverted structures based on the current direction. The inverted structure, widely adopted for its higher stability,[6] is commonly fabricated in sequence of electron transport layer (ETL), photoactive layer (PAL), and hole transport layer (HTL). For HTL fabrication, the vacuum-based approach, typically exemplified by the vacuum thermal evaporation of MoO_3, offers precise controllability and high repeatability, making it a reliable choice for device fabrication.[7] On the other hand, solution-processed HTL materials, such as $HMoO_x$ nanoparticle,[8] MoO_3:PEDOT:PSS,[9] conjugated polymers,[10] polyoxometalates (POMs),[11] and POM:PEDOT:PSS composites,[12] provide excellent compatibility and scalability with large-scale roll-to-roll printing processes.

In 2017, Kolesov et al. pioneered an immersion-based doping method to fabricate a HTL for OSCs by immersing the PAL-containing substrates in a nitromethane solution of phosphomolybdic acid (PMA). This process formed the HTL through the diffusion of PMA and the subsequent in situ doping of the PAL.[13] A power conversion efficiency (PCE) of 4.8% in P3HT:ICBA-based devices was achieved, surpassing that of reference devices using evaporated MoO_3 as the HTL. This approach provided a novel pathway for utilizing high oxidation state Mo-doped semiconductor phases.[13] Building on this foundational work and conforming to the ever-developed donor and acceptor semiconductors, subsequent studies sought to optimize the PMA doping method to have a better understanding of doping mechanisms and achieve higher OSCs performance.

To mitigate the safety concerns associated with explosive solvent nitromethane, researchers transitioned to air-stable solvents, such as acetonitrile (ACN), which facilitated the intercalation of PMA between the lamellae of P3HT while preserving the integrity of $\pi-\pi$ stacking. This solvent substitution, applied to the same P3HT:ICBA system, yielded

Received: May 27, 2025
Revised: June 22, 2025
Accepted: June 25, 2025
Published: July 3, 2025

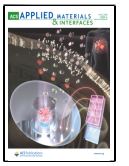

https://doi.org/10.1021/acsami.5c10367
ACS Appl. Mater. Interfaces 2025, 17, 40605−40612

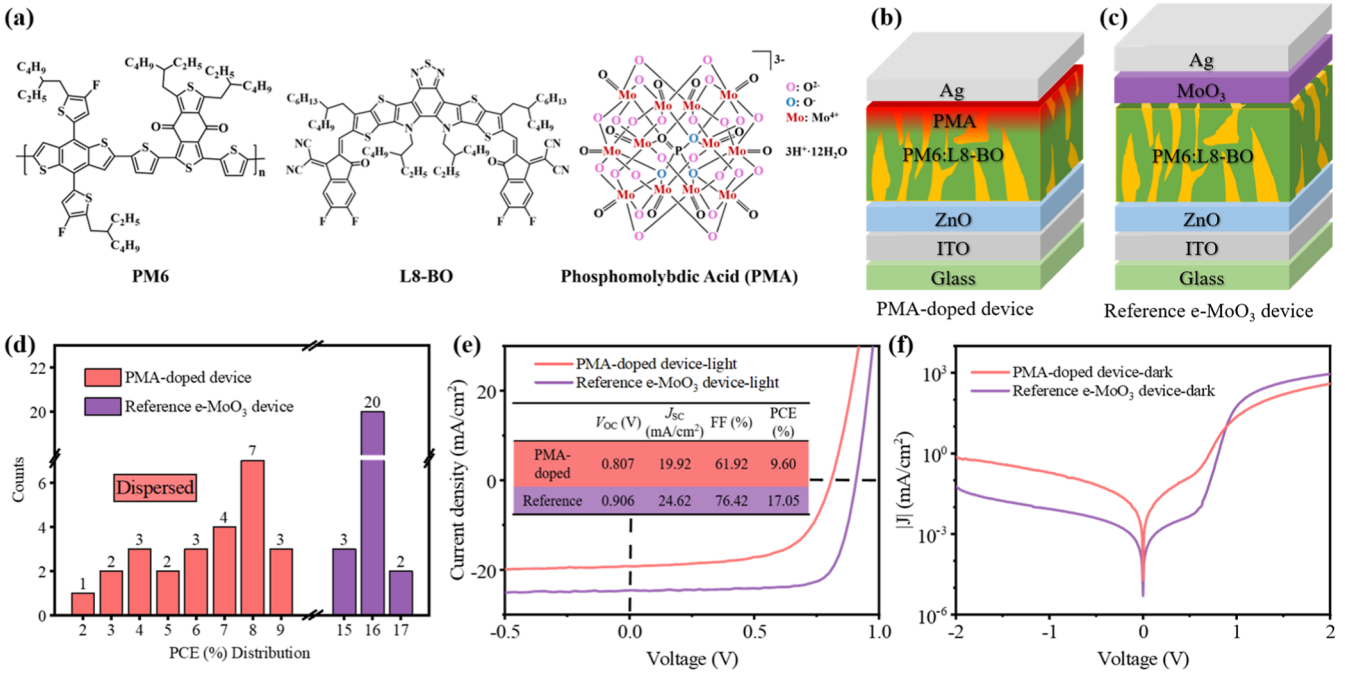

Figure 1. (a) Chemical structures of PM6, L8-BO, and PMA; (b,c) OSC device structures of (b) PMA-doped device and (c) reference e-MoO_3 device; (d) histogram of PCE distribution for 25 PMA-doped devices and 25 reference e-MoO_3 devices; (e,f) $J-V$ characteristics of the best-performed devices of PMA-doped device and reference e-MoO_3 device: (e) light curves and inset table summarizing the photovoltaic parameters; and (f) dark curves.

a further improvement in PCE to 5.4%.[14] Further advancements in the field were achieved through the introduction of binary solvent systems and solvent vapor pretreatment methodologies. Specifically, the incorporation of 1,2-dichlorobenzene as a cosolvent enabled deeper PMA infiltration into the PAL, expanding its applicability to the PBDB-T:IEICO-4F system. This strategy resulted in a significant upward shift in the Fermi level up to 0.33 eV and a corresponding PCE of 8.2%, underscoring the role of solvent engineering in enhancing device performance.[15] A critical parameter influencing device efficiency was identified in a subsequent study, which demonstrated that immersion time directly impacts PMA penetration depth and, consequently, device performance. When optimized to 3 min doping, PTB7-Th:IEICO-4F-based devices achieved a record PCE of 11.37%, marking the highest reported efficiency for PMA-doped single-junction OSCs.[16] Collectively, these findings highlight the importance of doping kinetics in tailoring the properties of PMA-doped PAL and optimizing charge transport pathways and also illustrate the evolution of PMA doping strategies from simple immersion techniques to solvent-engineered approaches, driving sustained improvements in OSCs device performance.

Significant progress has been made in optimizing the PMA doping method and enhancing OSCs device performance. However, recent studies have highlighted the critical role of HTL material diffusion within the PAL, influencing device performance and stability.[17,18] It is thus important to investigate the diffusion behavior of PMA within the PAL. Motivated by these observations, this study investigates PMA diffusion kinetics in both surface and depth directions within the state-of-the-art PM6:L8-BO system.[19−21] We propose a novel two-step spin-rinsing technique following the PMA doping process, which enhances lateral homogeneity as confirmed by the laser beam-induced current (LBIC) imaging measurement. Meanwhile, time-of-flight secondary ion mass spectrometry (ToF-SIMS) analysis revealed excessive depth diffusion of PMA, particularly within the thinner PAL. To address this issue, we introduced thicker PAL configurations and analyzed the PAL absorption spectrum and vertical phase separation behavior to elucidate the diffusion mechanism.

2. RESULTS AND DISCUSSION

2.1. PMA-Doped PM6:L8-BO Device Performance. We first studied the application of PMA doping methods in the PM6:L8-BO system (Figure 1a). The reference devices are prepared according to a common method, in which MoO_3 is deposited via vacuum thermal evaporation as the HTL (Figure 1c). PMA-doped devices are prepared according to the structure shown in Figure 1b, where in the final step of the PMA doping process, the PMA residual is removed under a one-step spin-rinsing technique. Additionally, apart from the HTL, the thickness of other layers, particularly for PAL, is maintained identical between doped and reference devices.[13,14,16] The PAL thickness was set to 98 nm, determined based on the optimal performance achievable by the reference devices.

Statistical results shown in Figure 1d indicated that the PCE of the reference devices primarily fell within the range 15−17%, attributed to the precise controllability and high stability of the vacuum thermal evaporation technique. In contrast, the PCE of doped devices varied from 2% to 9%, not only lower than the reference devices but also lacking repeatability. Figure 1e,f presents the current density−voltage ($J-V$) curves under light and dark conditions for the best-performed devices of both types, with key photovoltaic parameters summarized in an inset table in Figure 1e. The photovoltaic performance of the reference device was comparable with values reported in the literature.[19] However, the doped device exhibited suboptimal photovoltaic performance when compared with the reference

https://doi.org/10.1021/acsami.5c10367
ACS Appl. Mater. Interfaces 2025, 17, 40605−40612

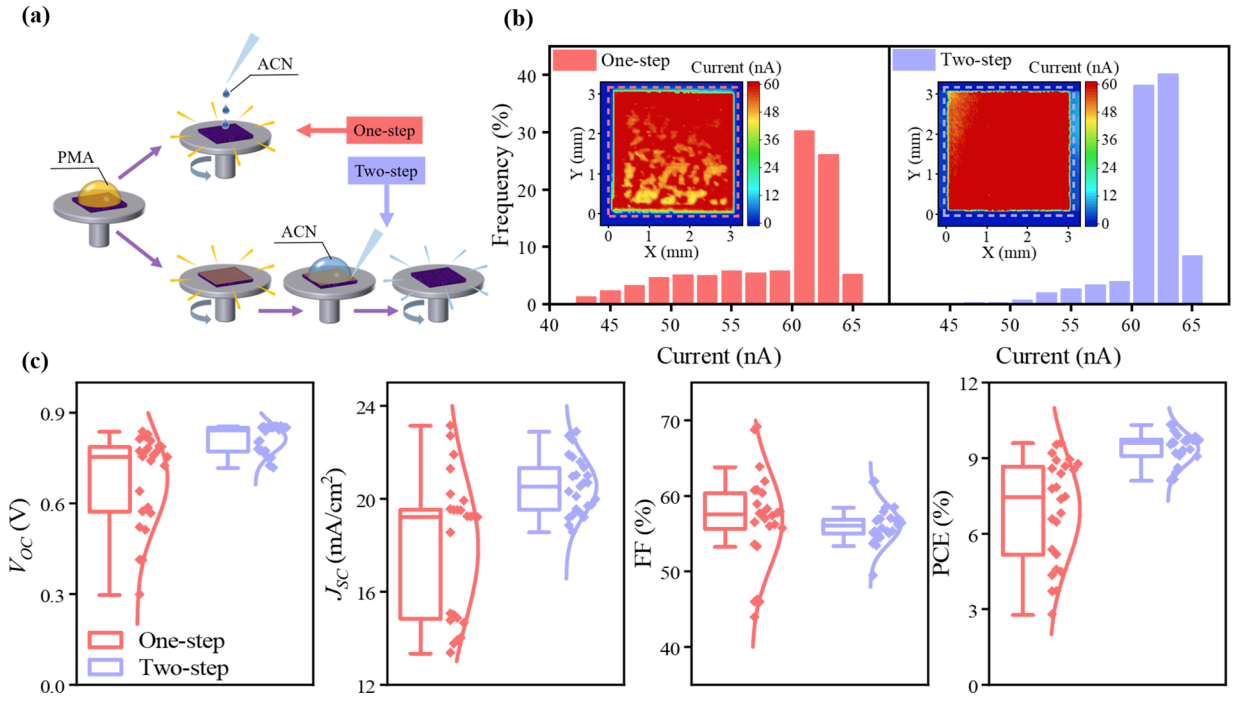

Figure 2. (a) Schematic diagram of the one-step and two-step spin-rinsing technique. (b) Frequency distribution of photocurrent for two individual devices fabricated using the one-step and two-step spin-rinsing technique, with inset LBIC images of representative devices and outlined effective area. (c) Box plots of performance parameters (V_{OC}, J_{SC}, FF, PCE) distribution of 25 doped devices fabricated using the one-step and two-step spin-rinsing technique.

device. The open-circuit voltage (V_{OC}) of the doped device was 0.807 V, which is lower than that of the reference device (0.906 V). This may possibly imply an energy-level mismatch at the PMA/PAL interface. The short-circuit current density (J_{SC}) of the doped device was 19.92 mA/cm^2, compared to the standard device's 24.62 mA/cm^2, which could perhaps indicate some hindrance to carrier transport and extraction. Additionally, the fill factor (FF) of the doped device was 61.92%, while the reference device achieved 76.42%, suggesting that there might be increased exciton recombination in the doped device. Furthermore, analysis of the dark curves revealed that the doped device exhibited a reduced difference between forward and reverse bias, indicative of a higher leakage current. This observation is consistent with the diminished diode characteristics and reduced conductivity, which was also corroborated by the lower J_{SC} measured under illumination.[22] Moreover, the doped device demonstrated a lower dark saturation current under reverse bias, which is attributed to a reduced density of trap and midgap states.[23] The fitting results of the dark curves are shown in Figure S1, and the resulting parameters are given in Table S1. Higher diode ideality factor (n) and bias saturation current density (J_0) stands for higher recombination and higher series resistance (R_s) means blocked charge extraction and transportation.

Based on the results of device fabrication repeatability and photovoltaic performance, it was concluded that this traditional PMA doping method commonly reported in the literature may have potential limitations in the PM6:L8-BO system. Therefore, it is necessary to optimize the fabrication technique and investigate how the PMA diffusion behavior affects device performance.

2.2. Homogeneity Manipulation from Surface Direction. To investigate how the one-step spin-rinsing technique (Top path in Figure 2a) affects the PMA-doped PAL morphology, LBIC imaging, which can directly scan the entire device to obtain the magnitude of the photocurrent at each position in the 2D plane and thereby reflect the uniformity of the device's optoelectronic properties, was employed to visualize the current distribution in the surface direction, as shown in the schematic diagram in Figure S2a. The LBIC image for one representative doped device, shown in the left inset plot of Figure 2b, revealed an inhomogeneous current distribution, which likely contributes to the low repeatability of device performance and the low efficiency. Quantitative analysis (left panel of Figure 2b) of the current frequency distribution within the effective area (outlined by the dashed frame in the LBIC image) indicated that only about 60% of the area displayed higher photocurrents (>60 nA). Additional LBIC images for devices fabricated under the same one-step spin-rinsing technique have shown similar inhomogeneities (Figure S2b).

To address this issue, a novel two-step spin-rinsing technique was proposed, as illustrated in the bottom path of Figure 2a. After the preliminary spin-off of the residual PMA solution, the solvent and spin-off are spread immediately. This technique was designed to minimize potential damage to the doped PAL compared with the one-step technique. As shown in the right panel of the inset in Figure 2b, the LBIC image indicates that the homogeneity along the surface direction is enhanced. Specifically, the proportion of the effective area with a current greater than 60 nA increased to 90%. Likewise, additional LBIC images for devices fabricated under the two-step spin-rinsing technique are presented in Figure S2c.

To evaluate the impact of the two-step spin-rinsing technique on device repeatability, another 25 doped devices were fabricated, and their performance distribution was statistically analyzed in Figure 2c. The photovoltaic parameters of these devices were compared with those fabricated using a

https://doi.org/10.1021/acsami.5c10367
ACS Appl. Mater. Interfaces 2025, 17, 40605−40612

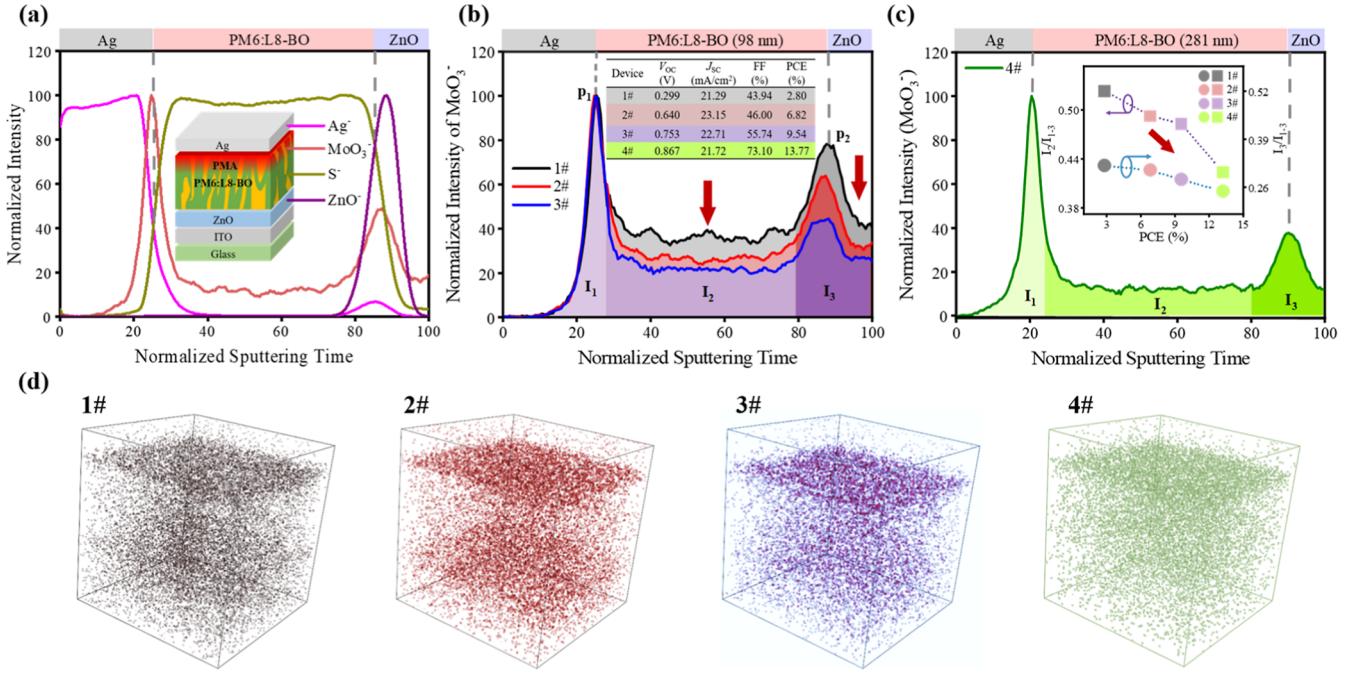

Figure 3. ToF-SIMS characterization: (a) generalized position indication of device layers: Ag^- for Ag anode, MoO_3^- for PMA, S^- for PAL, and ZnO^- for ZnO electron transport layer; (b) PMA distribution in three devices with same 98 nm PAL but varying performance, where MoO_3^- represents PMA. For clarity, sputtering time and absolute intensity are normalized to the range of 0−100. I_1, I_2, and I_3 stand for the integral areas of PMA enrichment at the Ag/PAL interface, PAL bulk, and PAL/ZnO interface, respectively. The inset table lists the photovoltaic parameters of the four characterized devices, with the performance of devices 1#−4# increasing in sequence; (c) PMA distribution of the champion device with 281 nm PAL, with the inset showing the trends of I_2/I_{1-3} and I_3/I_{1-3} of four devices with different performance; and (d) 3D render overlay of MoO_3^- for the four devices.

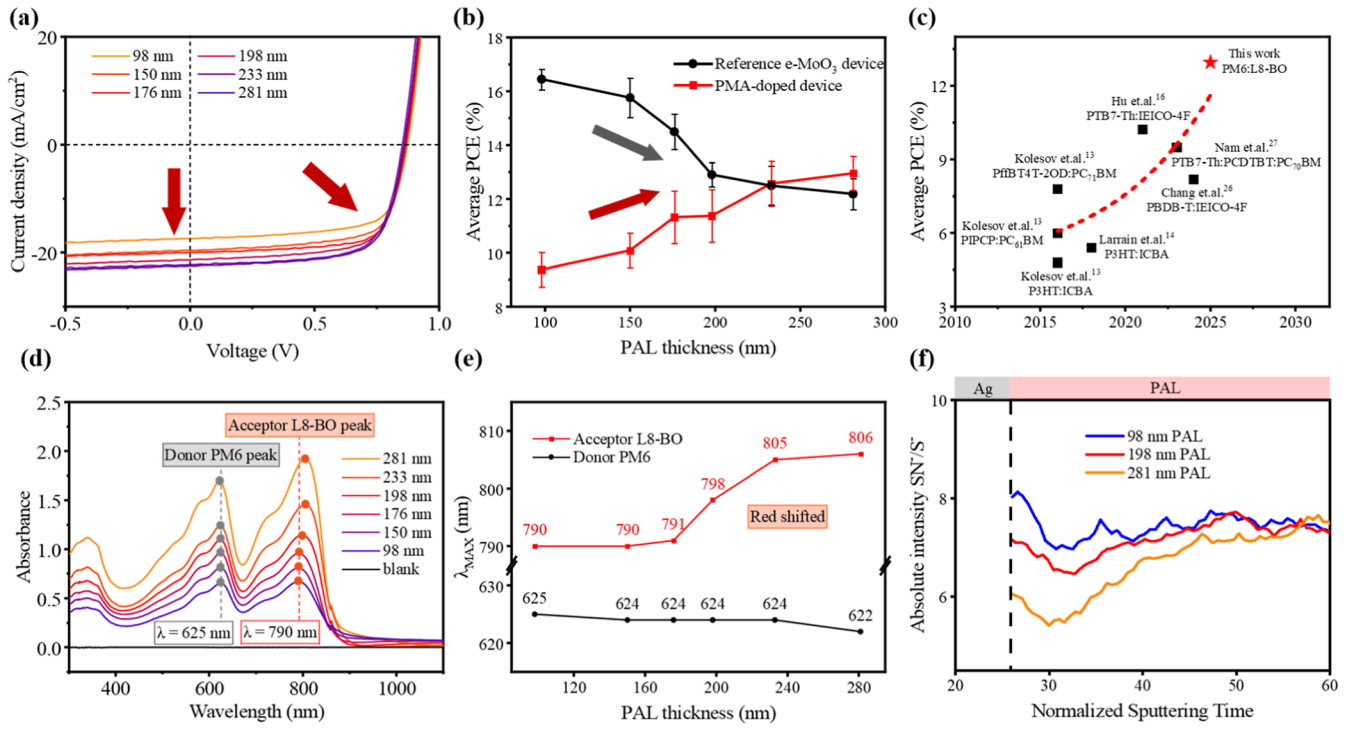

Figure 4. (a) $J-V$ characteristics of best-performed PMA-doped device with gradient PAL thickness; (b) average PCE evolution of both PMA-doped and reference e-MoO_3 devices under different PAL thickness; (c) best performance record of single-junction OPV fabricated using the PMA doping method; (d) absorption spectra of the PM6:L8-BO film with gradient thickness; (e) maximum absorbance peak wavelength shifting of PM6 and L8-BO; and (f) ToF-SIMS characterization representing the relative content of L8-BO and PM6 through PAL with 98, 198, and 281 nm.

one-step technique previously noted in Figure 1d. The results demonstrated that devices fabricated using the two-step technique exhibited higher consistency in all photovoltaic parameters and slightly improved performance (PCE of 8−

https://doi.org/10.1021/acsami.5c10367
ACS Appl. Mater. Interfaces 2025, 17, 40605−40612

10%). This improvement may be attributed to avoiding inhomogeneous rinsing caused by intense dynamic spinning. Overall, the two-step spin-rinsing technique was found to enhance doping controllability and repeatability from the surface direction.

2.3. Depth Diffusion of PMA in PAL. Our recent study has shown that during the fabrication of reference devices, MoO_3 will diffuse through the PAL, reaching the PAL/ZnO interface during the vacuum thermal evaporation process. This diffusion leads to the formation of a highly concentrated negative charge region at the PAL/ZnO interface, which increases the electron injection barrier at this interface, thereby deteriorating the performance and thermal stability.[18] Inspired by this discovery, we would like to investigate how, in the solution-based methods, the PMA diffusion behavior within the PAL affects the performance of devices.

To investigate this, three independent devices with significant performance variations (1#−3#, inset table of photovoltaic parameters in Figure 3b) were selected and characterized using ToF-SIMS, with results shown in Figure 3a,b, and 3D rendering overlay of MoO_3^- is displayed in Figure 3d (1#−3#). Surprisingly, PMA was found to enrich not only at the Ag/PAL interface (p_1) but also at the PAL/ZnO interface (p_2). Although this shows some similarities with our previous studies, which use evaporated MoO_3,[17,18] the much higher intensity of the MoO_3^- signal in the PAL region and at the PAL/ZnO interface cannot primarily be attributed to the tailing effect. Therefore, integral region ratios I_2/I_{1-3} and I_3/I_{1-3} of MoO_3^- were used to quantify the relative amount of PMA remaining in the PAL bulk and its enrichment at the PAL/ZnO interface. As indicated by the red arrow in Figure 3b and the variation of integral ratios in the inset of Figure 3c, device performance improved with decreasing I_2/I_{1-3} and I_3/I_{1-3}, suggesting that excessive PMA retention in the PAL bulk and its enrichment at the PAL/ZnO interface negatively impact device performance. PMA exhibits high compatibility between its LUMO level (−5.21 eV) and the HOMO level (−5.54 eV) of PM6,[24] and it also has high electron affinity and strong oxidation capacity.[11] Therefore, its excessive presence inside the bulk PAL and the PAL/ZnO interface will block electron transportation. Thus, minimizing PMA retention in the PAL bulk (I_2/I_{1-3}) and its enrichment at the PAL/ZnO interface (I_3/I_{1-3}) while maintaining effective doping at the Ag/PAL interface (p_1 and I_1) is crucial for performance optimization.

2.4. Diffusion Manipulation from Depth Direction. To address the challenge of material interdiffusion in photovoltaics, prior studies have demonstrated that forming a diffusion barrier or extending the diffusion length by incorporating less penetrable buffer layers can effectively mitigate interdiffusion.[18,25] Inspired by these strategies and motivated by the demand for thicker films in industrial printing processes, we investigated the effect of the PAL thickness on the PMA diffusion.

The $J-V$ characteristics of best-performed doped devices with varied PAL thicknesses are presented in Figure 4a, and the average PCE evolution of both PMA-doped and reference e-MoO_3 devices under different PAL thickness is summarized in Figure 4b. Additional evolutional curves for photovoltaic parameters (V_{OC}, J_{SC}, and FF) and detailed data are provided in Figure S3 and Table S2. The results indicate that increasing the PAL thickness from 98 to 281 nm significantly enhances the device performance. Specifically, the V_{OC} improved by approximately 0.05 V, suggesting enhanced interfacial energy-level alignment. The J_{SC} increased by about 2 mA/cm^2, reflecting improved carrier transport and extraction and also higher conductivity. Most notably, the FF increased from 56% to 70%, indicating a significant reduction in exciton recombination within the device. Consequently, the PCE improved from 9.38% to 12.96%, achieving comparable performance to reference devices with equivalent PAL thickness. Here, the best-performed doped device (4#) with a 281 nm PAL was characterized by ToF-SIMS, and the distribution of PMA is shown in Figure 3c and the fourth 3D overlay of Figure 3d. The green points in the inset of Figure 3c show reduced I_2/I_{1-3} and I_3/I_{1-3}, confirming that increasing the thickness of PAL effectively extends the diffusion length of PMA, thereby suppressing its excessive diffusion. To the best of our knowledge, in the subfield of PMA-doped single-junction OPV, we have achieved the highest performance to date, with a PCE of 12.96 ± 0.62% (champion device at 13.77%). Additionally, we have constructed a performance evolution map (Figure 4c) of this subfield that summarizes the highest efficiencies over the years; detailed photovoltaic parameters are listed in Table S3.

To investigate the underlying mechanisms of how thicker PAL impedes PMA diffusion, we first obtained UV−vis−NIR spectra (Figure 4d) of neat PM6:L8-BO films with varying thicknesses. The maximum absorption peaks ($\lambda_{max,ab}$) of PM6 and L8-BO are around 625 and 790 nm, respectively, which aligns with previous reports.[19,21] The $\lambda_{max,ab}$ values for PM6 and L8-BO corresponding to different film thicknesses are summarized in Figure 4e. As the film thickness increases from 98 to 281 nm, the $\lambda_{max,ab}$ of PM6 exhibits a slight blue shift, while the $\lambda_{max,ab}$ of L8-BO undergoes a significant red shift from 790 to 806 nm. This is probably attributed to increased $\pi-\pi$ stacking overlaps, which enhance intermolecular interactions and lead to stronger electronic coupling between L8-BO monomers.[19] This stronger effect likely creates a more stable molecular network, which effectively hinders the excessive diffusion of PMA. Subsequently, ToF-SIMS was employed to observe the vertical phase separation of three representative thicknesses (98, 198, and 281 nm), as shown in Figure 4f. Since the SN^- signal originates from L8-BO and the S^- signal primarily arises from PM6, the observed decrease in the SN^-/S^- ratio of thicker PAL film reflects a reduced acceptor concentration near the Ag/PAL interface. This apparent vertical phase separation may also contribute to slowing excessive PMA diffusion and enhance charge extraction, which reduces recombination and energy loss, reflected by a significant increase of FF from 56% to 70%.

To sum up, the observed performance enhancement from increasing PAL thickness is not only attributed to the extended PMA diffusion distance. Alterations in the stacking arrangement of the organic semiconductor molecules as well as changes in vertical phase separation likely played a significant role. These factors collectively influence the overall performance of the device.

3. CONCLUSIONS

An investigation was conducted into the suboptimal performance of the traditional PMA doping method within the PM6:L8-BO system. The issues were categorized into two aspects: the uneven surface distribution of PMA and its excessive depth diffusion. We developed a novel two-step spin-rinsing technique that enhances fabrication repeatability and

https://doi.org/10.1021/acsami.5c10367
ACS Appl. Mater. Interfaces 2025, 17, 40605−40612

doping uniformity compared to the traditional one-step method, yielding a narrower PCE distribution (8−10% vs 2−9%) and increasing the relative area of the higher photocurrent (>60 nA) from 60% to 90%. Furthermore, by increasing the PAL thickness to 281 nm, we achieved a PCE of 12.96 ± 0.62% (with a champion device at 13.77%), marking the highest PCE record in PMA-doped single-junction OSCs. This improvement may be attributed to two key factors: stronger intermolecular interactions of L8-BO in thicker films, which stabilize molecular networks, and enhanced charge extraction, which reduces recombination and energy loss. These findings highlight the importance of refining doping processes and optimizing film characteristic to regulate dopant diffusion as key strategies for enhancing the performance of OSCs.

However, the performance of thicker film doped devices still has a PCE gap of approximately 4% compared with that of thinner film reference devices with evaporated MoO_3. In future research, from a theoretical perspective, the diffusion of PMA should be further controllable by some new strategies, such as inserting a barrier layer, and the underlying mechanisms also should be investigated in detail to obtain the best PMA diffusion degree. From a technological perspective, developing more continuous and uniform immersion doping processes and rinsing processes, such as the combination of a roll-to-roll production line with tanks of PMA solution and rinsing solvent, may be an effective way to improve the uniformity and efficiency of the devices.

4. EXPERIMENTAL SECTION

4.1. OSC Device Fabrication. (1) Customized glass substrates with patterned ITO were first cleaned by wiping with a dust-free cloth soaked in detergent, followed by ultrasonic cleaning in deionized water and ethanol for 30 min each, repeated twice for each solvent. The substrates were dried by blowing with clean N_2 and subjected to UV−ozone treatment for 30 min to ensure surface cleanliness and compatibility with following layers. (2) A ZnO precursor solution was prepared by first dissolving 1200 mg of zinc acetate dihydrate (Shanghai Titan Scientific Co., Ltd.) in 300 μL of deionized water, followed by complete dissolution in a 20 mL solution of 0.5 wt % polyethylenimine (Sigma-Aldrich) solution in 2-methoxyethanol (J&K Scientific). The filtered precursor solution was spin-coated onto the glass/ITO substrates and annealed at 200 °C for 30 min to form a crystalline ZnO electron transport layer (ETL). (3) In a N_2-filled glovebox, PM6 (Organtec Ltd.), L8-BO (Hyper Inc.), and 1,4-Diiodobenzene (TCI) were dissolved in chloroform (ADAMAS-BETA Inc.) at a mass ratio of 1.0:1.2:1.1. Different-thickness photoactive layers (PALs) were deposited by varying the PM6 concentration to 8, 9, 10, 11, 12, and 13 mg/mL, respectively, while maintaining a fixed spin-coating speed of 1500 r.p.m. The films were annealed on a hot plate at 85 °C for 5 min. (4) The hole transport layer (HTL) was prepared using two methods: PMA doping was used for doped devices and vacuum thermal evaporation was used for reference devices. For the PMA doping method, the PAL surface was coated with 500 μL of a 50 mg/mL PMA (Thermo Scientific) solution in acetonitrile (Fisher Chemical) for 60 s. In the one-step spin-rinsing process, the surface was rinsed with acetonitrile at 3000 rpm to remove PMA residues. In the two-step spin-rinsing process, the PMA solution was spin-coated and dried to ensure complete solvent evaporation, followed by slow edge-to-center tiling with pure acetonitrile until the PAL was fully covered, and then spun at 3000 rpm to achieve a uniformly doped surface. Reference devices were fabricated using a 10 nm MoO_3 layer deposited via vacuum thermal evaporation as the hole transport layer. (5) A 120 nm Ag layer was evaporated as the top anode.

4.2. Characterization. *4.2.1. OSCs Device Characterization.* (1) The $J-V$ curves of the OSC devices (with a well-defined 0.0625 cm^2 aperture) were recorded under AM 1.5G illumination (XES-40S3 solar simulator, 100 mW/cm^2) using a digital source meter (Keithley 2400). Key parameters, including open circuit voltage (V_{OC}), short circuit current density (J_{SC}), fill factor (FF), and power conversion efficiency (PCE), were extracted from the recorded curves. (2) The schematic diagram of the LBIC method is shown in Figure S2a. A focused visible laser beam (532 nm, 20 μm diameter) was incident on the complete device from the glass side, and the generated photocurrent was collected via an external circuit. The beam scanned the device surface in an S-shaped path with a step width of 100 μm. The distribution of the photocurrent was visualized as contour plots to obtain the LBIC image. The device samples underwent $J-V$ testing to ensure the effectiveness of their performance. (3) The depth profiling of the device was performed using ToF-SIMS. A sputtering ion beam was incident from the Ag side, and the device was etched layer by layer. The absolute intensities of various ion fragments were monitored as a function of the sputtering time. The sputtering area was 0.04 mm^2, and data were collected in anion mode.

4.2.2. PM6:L8-BO Film Characterization. (1) The absorbance spectra of the films were recorded using a UV−vis−NIR spectrometer (PerkinElmer Lambda 750) over the wavelength range of 300−1100 nm. The measurements were performed based on glass/ZnO substrates, where the ZnO layer was used to ensure compatibility between the PM6:L8-BO film and the glass substrate. (2) Film thicknesses were determined using a profilometer (KLA Tencor P-7). The tip force was 2 mg and the measurement speed was 100 μm/s. Each measurement was repeated twice to ensure accuracy.

■ ASSOCIATED CONTENT

Supporting Information

The Supporting Information is available free of charge at https://pubs.acs.org/doi/10.1021/acsami.5c10367.

Fitting of dark $J-V$ curves: dV/dJ vs $(J - J_{SC})^{-1}$ and $\ln(J - J_{SC})$ vs $V - R_sJ$ with inserted corresponding formula, fitting results (n, R_s, J_0) summary of the best-performed doped and reference device, schematic diagram of the LBIC method and LBIC images of 3 individual devices fabricated using the one-step and two-step spin-rinsing technique, photovoltaic parameters of PM6:L8-BO devices with different PAL thicknesses, performance parameters (V_{OC}, J_{SC}, and FF) evolution of both the reference e-MoO_3 device and the PMA-doped device under different PAL thicknesses, and recent progress of inverted OSCs fabricated under the PMA doping method (PDF)

■ AUTHOR INFORMATION

Corresponding Authors

Yi Lin − *School of Science, Department of Chemistry and Materials Science, Xi'an Jiaotong-Liverpool University, Suzhou 215123, P. R. China;* orcid.org/0000-0001-9478-152X; Email: Yi.Lin@xjtlu.edu.cn

Chang-Qi Ma − *i-Lab & Printable Electronics Research Center, Suzhou Institute of Nano-Tech and Nano-Bionics, Chinese Academy of Sciences, Suzhou 215123, P. R. China;* orcid.org/0000-0002-9293-5027; Email: cqma2011@sinano.ac.cn

Authors

Jinlong Wu − *School of Science, Department of Chemistry and Materials Science, Xi'an Jiaotong-Liverpool University, Suzhou 215123, P. R. China; i-Lab & Printable Electronics Research Center, Suzhou Institute of Nano-Tech and Nano-*

https://doi.org/10.1021/acsami.5c10367
ACS Appl. Mater. Interfaces 2025, 17, 40605−40612

Bionics, Chinese Academy of Sciences, Suzhou 215123, P. R. China

Qian Xi − *i-Lab & Printable Electronics Research Center, Suzhou Institute of Nano-Tech and Nano-Bionics, Chinese Academy of Sciences, Suzhou 215123, P. R. China*

Na Wu − *i-Lab & Printable Electronics Research Center, Suzhou Institute of Nano-Tech and Nano-Bionics, Chinese Academy of Sciences, Suzhou 215123, P. R. China*

Rong Huang − *Vacuum Interconnected Nanotech Workstation, Suzhou Institute of Nano-Tech and Nano-Bionics, Chinese Academy of Sciences (CAS), Suzhou 215123, P. R. China*

Complete contact information is available at: https://pubs.acs.org/10.1021/acsami.5c10367

Notes

The authors declare no competing financial interest.

■ ACKNOWLEDGMENTS

The authors sincerely express gratitude to the Xi'an Jiaotong-Liverpool University Postgraduate Research Scholarship Foundation (PGRS1912016 and FOSA2206023) and Chinese Academy of Sciences (Grant No. YJKYYQ20180029) for their financial support. The authors would also like to thank the technical support for Nano-X from Suzhou Institute of Nano-Tech and Nano-Bionics, Chinese Academy of Science.

■ REFERENCES

(1) Xu, Z.; Xu, G.; Luo, Q.; Han, Y.; Tang, Y.; Miao, Y.; Li, Y.; Qin, J.; Guo, J.; Zha, W.; Gong, C.; Lu, K.; Zhang, J.; Wei, Z.; Cai, R.; Yang, Y.; Li, Z.; Ma, C.-Q. *In Situ* Performance and Stability Tests of Large-Area Flexible Polymer Solar Cells in the 35-Km Stratospheric Environment. *Natl. Sci. Rev.* **2023**, *10*, nwac285.

(2) Guo, J.; Min, J. A Cost Analysis of Fully Solution-Processed ITO-Free Organic Solar Modules. *Adv. Energy Mater.* **2019**, *9*, 1802521.

(3) Wang, G.; Adil, M. A.; Zhang, J.; Wei, Z. Large-Area Organic Solar Cells: Material Requirements, Modular Designs, and Printing Methods. *Adv. Mater.* **2019**, *31*, 1805089.

(4) Yang, S.; Chen, X.; Pan, Y.; Fang, J.; Han, Y.; Wang, Z.; Qian, F.; Qi, W.; Shui, K.; Zhang, Q.; Guo, F.; Sun, Y.; Ma, C.; Luo, Q. High Cell to Module Efficiency Remaining Ratio of ≈90% for the 100 Cm^2 Fully Roll-to-Roll Gravure Printed Flexible Organic Solar Cells From Non-Halogenated Solvent. *Adv. Mater.* **2025**, *37*, 2500115.

(5) Solak, E. K.; Irmak, E. Advances in Organic Photovoltaic Cells: A Comprehensive Review of Materials, Technologies, and Performance. *RSC Adv.* **2023**, *13*, 12244−12269.

(6) Liu, B.; Sandberg, O. J.; Qin, J.; Liu, Y.; Wilken, S.; Wu, N.; Yu, X.; Fang, J.; Li, Z.; Huang, R.; Zha, W.; Luo, Q.; Tan, H.; Österbacka, R.; Ma, C.-Q. Inverted Organic Solar Cells with an in Situ-Derived SiOxNy Passivation Layer and Power Conversion Efficiency Exceeding 18%. *Nat. Photonics* **2025**, *19*, 195−203.

(7) Chen, B.-W.; An, M.-W.; Wang, K.; Jeong, S. Y.; Wang, X.; Qiu, Z.-L.; Cao, K.; Zheng, S.-Y.; Wang, L.; Woo, H. Y.; Yun, D.-Q.; Deng, L.-L.; Xie, S.-Y.; Zheng, L.-S. Unprecedented Short-Circuit Current Density and Efficiency of Vacuum-Deposited Organic Solar Cells Based on 8*H*-Thieno[2′,3′:4,5]Thieno[3,2-*b*] Thieno[2,3-*d*]Pyrrole. *Sci. Bull.* **2025**, *70*, 897−904.

(8) Zha, W.; Gu, H.; Pan, W.; Sun, X.; Han, Y.; Li, Z.; Weng, X.; Luo, Q.; Yang, S.; Ma, C.-Q. Controllable Synthesis and N-Doping of HMoOx Nanoparticle Inks through Simple Photoreduction for Solution-Processed Organic Photovoltaics. *Chem. Eng. J. Adv.* **2021**, *425*, 130620.

(9) Wang, Y.; Luo, Q.; Wu, N.; Wang, Q.; Zhu, H.; Chen, L.; Li, Y.-Q.; Luo, L.; Ma, C.-Q. Solution-Processed MoO_3:PEDOT:PSS Hybrid Hole Transporting Layer for Inverted Polymer Solar Cells. *ACS Appl. Mater. Interfaces* **2015**, *7*, 7170−7179.

(10) Zhou, H.; Zhang, Y.; Mai, C.; Collins, S. D.; Nguyen, T.; Bazan, G. C.; Heeger, A. J. Conductive Conjugated Polyelectrolyte as Hole-Transporting Layer for Organic Bulk Heterojunction Solar Cells. *Adv. Mater.* **2014**, *26*, 780−785.

(11) Tong, Y.; Xu, B.; Ye, F. Recent Advance in Solution-Processed Hole Transporting Materials for Organic Solar Cells. *Adv. Funct. Mater.* **2024**, *34*, 2310865.

(12) Ji, G.; Wang, Y.; Luo, Q.; Han, K.; Xie, M.; Zhang, L.; Wu, N.; Lin, J.; Xiao, S.; Li, Y.-Q.; Luo, L.-Q.; Ma, C.-Q. Fully Coated Semitransparent Organic Solar Cells with a Doctor-Blade-Coated Composite Anode Buffer Layer of Phosphomolybdic Acid and PEDOT:PSS and a Spray-Coated Silver Nanowire Top Electrode. *ACS Appl. Mater. Interfaces* **2018**, *10*, 943−954.

(13) Kolesov, V. A.; Fuentes-Hernandez, C.; Chou, W.-F.; Aizawa, N.; Larrain, F. A.; Wang, M.; Perrotta, A.; Choi, S.; Graham, S.; Bazan, G. C.; Nguyen, T.-Q.; Marder, S. R.; Kippelen, B. Solution-Based Electrical Doping of Semiconducting Polymer Films over a Limited Depth. *Nat. Mater.* **2017**, *16*, 474−480.

(14) Larrain, F. A.; Fuentes-Hernandez, C.; Chou, W.-F.; Rodriguez-Toro, V.; Huang, T.-Y.; Toney, M. F.; Kippelen, B. Stable Solvent for Solution-Based Electrical Doping of Semiconducting Polymer Films and Its Application to Organic Solar Cells. *Energy Environ. Sci.* **2018**, *11*, 2216−2224.

(15) Larrain, F. A.; Fuentes-Hernandez, C.; Chang, Y.-C.; Rodriguez-Toro, V. A.; Abraham, S.; Kippelen, B. Increasing Volume in Conjugated Polymers to Facilitate Electrical Doping with Phosphomolybdic Acid. *ACS Appl. Mater. Interfaces* **2021**, *13*, 23260−23267.

(16) Hu, L.; You, W.; Sun, L.; Yu, S.; Yang, M.; Wang, H.; Li, Z.; Zhou, Y. Surface Doping of Non-Fullerene Photoactive Layer by Soluble Polyoxometalate for Printable Organic Solar Cells. *Chem. Commun.* **2021**, *57*, 2689−2692.

(17) Qin, X.; Yu, X.; Li, Z.; Fang, J.; Yan, L.; Wu, N.; Nyman, M.; Österbacka, R.; Huang, R.; Li, Z.; Ma, C.-Q. Thermal-Induced Performance Decay of the State-of-the-Art Polymer: Non-Fullerene Solar Cells and the Method of Suppression. *Molecules* **2023**, *28*, 6856.

(18) Xi, Q.; Qin, J.; Sandberg, O. J.; Wu, N.; Huang, R.; Li, Y.; Saladina, M.; Deibel, C.; Österbacka, R.; Ma, C.-Q. Improving the Thermal Stability of Inverted Organic Solar Cells by Mitigating the Undesired MoO_3 Diffusion toward Cathodes with a High-Ionization Potential Interface Layer. *ACS Appl. Mater. Interfaces* **2025**, *17*, 15456−15467.

(19) Li, C.; Zhou, J.; Song, J.; Xu, J.; Zhang, H.; Zhang, X.; Guo, J.; Zhu, L.; Wei, D.; Han, G.; Min, J.; Zhang, Y.; Xie, Z.; Yi, Y.; Yan, H.; Gao, F.; Liu, F.; Sun, Y. Non-Fullerene Acceptors with Branched Side Chains and Improved Molecular Packing to Exceed 18% Efficiency in Organic Solar Cells. *Nat. Energy* **2021**, *6*, 605−613.

(20) Yuan, J.; Zhang, Y.; Zhou, L.; Zhang, G.; Yip, H.-L.; Lau, T.-K.; Lu, X.; Zhu, C.; Peng, H.; Johnson, P. A.; Leclerc, M.; Cao, Y.; Ulanski, J.; Li, Y.; Zou, Y. Single-Junction Organic Solar Cell with over 15% Efficiency Using Fused-Ring Acceptor with Electron-Deficient Core. *Joule* **2019**, *3*, 1140−1151.

(21) Zhang, M.; Guo, X.; Ma, W.; Ade, H.; Hou, J. A Large-Bandgap Conjugated Polymer for Versatile Photovoltaic Applications with High Performance. *Adv. Mater.* **2015**, *27*, 4655−4660.

(22) Liu, Y.-F.; Zhang, S.-W.; Li, Y.-X.; Li, S.-L.; Huang, L.-Q.; Jing, Y.-N.; Cheng, Q.; Xiao, L.-G.; Wang, B.-X.; Han, B.; Kang, J.-J.; Zhang, Y.; Zhang, H.; Zhou, H.-Q. Solution-Processed Molybdenum Oxide Hole Transport Layer Stabilizes Organic Solar Cells. *Polym. Mater. Sci. Eng.* **2023**, *41*, 202−211.

(23) Sandberg, O. J.; Kaiser, C.; Zeiske, S.; Zarrabi, N.; Gielen, S.; Maes, W.; Vandewal, K.; Meredith, P.; Armin, A. Mid-Gap Trap State-Mediated Dark Current in Organic Photodiodes. *Nat. Photonics* **2023**, *17*, 368−374.

(24) Qu, M.; Li, Y.; Li, P.; Yang, X.; Wei, B.; Chen, G. Instability Mechanism of Phosphomolybdic Acid Solution and Its Effect on

Organic Solar Cells as a Hole-Transporting Layer. *Org. Electron.* **2023**, *120*, 106831.
(25) Wu, L.; Hu, S.; Yang, F.; Li, G.; Wang, J.; Zuo, W.; Jeronimo-Rendon, J. J.; Turren-Cruz, S.-H.; Saba, M.; Saliba, M.; Nazeeruddin, M. K.; Pascual, J.; Li, M.; Abate, A. Resilience Pathways for Halide Perovskite Photovoltaics under Temperature Cycling. *Nat. Rev. Mater.* **2025**, *8*, 137−146.

https://doi.org/10.1021/acsami.5c10367
ACS Appl. Mater. Interfaces 2025, 17, 40605−40612